



## Tibetan railway induced slight carbon loss: photosynthetic capacity decrease offsets growing season length increase in grasslands

Yajie Yang, Gaofei Yin, Jiangliu Xie, Rui Chen, Dujuan Ma, Changjing Wang, Guodong Zhang, Meilian Wang, Lu Zhou, Lin Huang, Qiaoyun Xie, Aleixandre Verger, Adrià Descals, Iolanda Filella & Josep Peñuelas

To cite this article: Yajie Yang, Gaofei Yin, Jiangliu Xie, Rui Chen, Dujuan Ma, Changjing Wang, Guodong Zhang, Meilian Wang, Lu Zhou, Lin Huang, Qiaoyun Xie, Aleixandre Verger, Adrià Descals, Iolanda Filella & Josep Peñuelas (2025) Tibetan railway induced slight carbon loss: photosynthetic capacity decrease offsets growing season length increase in grasslands, *International Journal of Digital Earth*, 18:2, 2554326, DOI: [10.1080/17538947.2025.2554326](https://doi.org/10.1080/17538947.2025.2554326)

To link to this article: <https://doi.org/10.1080/17538947.2025.2554326>



© 2025 The Author(s). Published by Informa UK Limited, trading as Taylor & Francis Group



[View supplementary material](#)



Published online: 23 Sep 2025.



[Submit your article to this journal](#)



Article views: 291



[View related articles](#)



[View Crossmark data](#)

# Tibetan railway induced slight carbon loss: photosynthetic capacity decrease offsets growing season length increase in grasslands

Yajie Yang<sup>a</sup>, Gaofei Yin<sup>a</sup>, Jiangliu Xie<sup>a</sup>, Rui Chen<sup>a</sup>, Dujuan Ma<sup>a</sup>, Changjing Wang<sup>a</sup>, Guodong Zhang<sup>a</sup>, Meilian Wang<sup>a</sup>, Lu Zhou<sup>b</sup>, Lin Huang<sup>c</sup>, Qiaoyun Xie<sup>d</sup>, Aleixandre Verger<sup>e,f</sup>, Adrià Descals<sup>f,g</sup>, Iolanda Filella<sup>f,g</sup> and Josep Peñuelas<sup>f,g</sup>

<sup>a</sup>Faculty of Geosciences and Engineering, Southwest Jiaotong University, Chengdu, People's Republic of China; <sup>b</sup>China Railway Eryuan Engineering Group CO., LTD, Chengdu, People's Republic of China; <sup>c</sup>Key Laboratory of Land Surface Pattern and Simulation, Institute of Geographic Sciences and Natural Resources Research, Chinese Academy of Sciences, Beijing, People's Republic of China; <sup>d</sup>School of Engineering, The University of Western Australia, Perth, Australia; <sup>e</sup>Centro de Investigaciones sobre Desertificación, CSIC-UV-GV, València, Spain; <sup>f</sup>Centre de Recerca Ecològica i Aplicacions Forestals, Barcelona, Spain; <sup>g</sup>CSIC, Global Ecology Unit CREAM-CSIC-UAB, Barcelona, Spain

## ABSTRACT

The Tibetan Railway has introduced pressures on the fragile grassland ecosystems of the Tibetan Plateau. However, the impact of the railway on the carbon sequestration remains unclear, as existing studies primarily focus on in-situ vegetation observations. In this study, we extracted the start and end of the growing season (SOS, EOS) and maximum daily GPP (GPPmax) along the railway corridor from the satellite-derived Gross Primary Productivity (GPP) data, and quantified the extent and intensity of the railway's disturbance on these indicators. We further employed the Statistical Model of Integrated Phenology and Physiology (SMIPP) to translate these disturbances into annual cumulative GPP (GPPann). Results show that Tibetan Railway significantly influences grassland within 50-meters, causing earlier SOS (0.1086 d m<sup>-1</sup>), delayed EOS (0.0646 d m<sup>-1</sup>), and reduced GPPmax (0.0069 gC m<sup>-2</sup> d<sup>-1</sup> m<sup>-1</sup>) as the distance to the railway gets closer. The advanced SOS and delayed EOS contributed gains of 28.82 and 104.26 MgC y<sup>-1</sup>, but reduction in GPPmax accounted for a loss of 2952.79 MgC y<sup>-1</sup>. Railway-induced phenology-physiology trade-off causes GPPann loss of 2819.71 MgC y<sup>-1</sup>. This study reveals Tibetan Railway's impact on grassland carbon cycling, offering insights for grassland conservation and sustainable transportation infrastructure projects.

## ARTICLE HISTORY

Received 13 April 2025  
Accepted 26 August 2025

## KEYWORDS

Tibetan Plateau; Tibetan railway; carbon sequestration; phenology; GPPmax

## 1. Introduction

Gross Primary Productivity (GPP) is a key indicator for measuring the carbon fixation capacity of terrestrial ecosystems (Anav et al. 2015). Therefore, accurate estimation of vegetation GPP is essential for understanding carbon cycle mechanisms and supporting sustainable development goals (Piao et al. 2009). The annual cumulative GPP (GPPann) of vegetation is influenced by both intrinsic plant attributes and environmental factors, which regulate plant phenology and physiological activities (Xie, Gu, and Yin 2024). Xia et al. (2015) decomposed GPPann into growing season length and photosynthetic capacity (represented by maximum daily GPP during the growing season, i.e. GPPmax), demonstrating that the combination of phenology and physiological processes effectively captures fluctuations in GPPann. The growing season length can be further partitioned into the start (SOS) and end (EOS) of the growing season; however, these two metrics exert distinct influences on carbon uptake. Studies have shown that SOS is closely correlated with spring GPP and EOS with autumn GPP (Keenan et al. 2014), while GPPmax is positively correlated with summer GPP (Stoy, Trowbridge, and Bauerle 2014). Therefore, SOS, EOS, and GPPmax influence carbon assimilation in different ways and are likely to have independent effects on GPPann. Based on this assumption,

**CONTACT** Gaofei Yin ✉ [yingf@swjtu.edu.cn](mailto:yingf@swjtu.edu.cn) Faculty of Geosciences and Engineering, Southwest Jiaotong University, Chengdu 610031, People's Republic of China

Supplemental data for this article can be accessed online at <https://doi.org/10.1080/17538947.2025.2554326>.

© 2025 The Author(s). Published by Informa UK Limited, trading as Taylor & Francis Group  
This is an Open Access article distributed under the terms of the Creative Commons Attribution License (<http://creativecommons.org/licenses/by/4.0/>), which permits unrestricted use, distribution, and reproduction in any medium, provided the original work is properly cited. The terms on which this article has been published allow the posting of the Accepted Manuscript in a repository by the author(s) or with their consent.

Zhou et al. (2016) proposed the Statistical Model of Integrated Phenology and Physiology (SMIPP) to quantitatively assess the contributions of SOS, EOS, and GPPmax to interannual GPPann variability.

Climate change has been demonstrated to exert profound impacts on the carbon sequestration capacity of terrestrial ecosystems (Beer et al. 2010). Shifts in temperature and precipitation patterns influence vegetation's ability to sequester carbon. For example, climate warming may result in an earlier SOS or delayed EOS in certain regions, enhancing carbon assimilation by vegetation (Keenan et al. 2014). However, excessive heat can inhibit photosynthetic enzyme activity, reducing photosynthesis and impairing carbon sequestration (Fang et al. 2024). In addition, extreme weather events (such as droughts, floods, heat waves, etc.) may also damage vegetation health and reduce its carbon sequestration capacity (Deng et al. 2021; Zeng et al. 2021). While these studies have significantly advanced our understanding of climate impacts on carbon dynamics, they predominantly focus on natural environmental changes, with limited attention to human-induced disturbances. The latter are a critical driver of structural and functional changes in terrestrial ecosystems in modern society, and their omission poses significant challenges to the accurate assessment of carbon balance (Running 2008).

The Tibetan Plateau, described as the 'Third Pole', supports the world's largest area of alpine grassland ecosystem (Cong et al. 2017). Covering over 60% of the plateau, these grasslands provide important ecological functions such as carbon storage, biodiversity conservation, and water resource regulation (Wang et al. 2022). The unique climatic conditions and variable topography of the Tibetan Plateau have resulted in a sensitive and fragile grassland ecological environment that is particularly vulnerable to human activities (Piao et al. 2009; Yao 2019). Consequently, the Tibetan Plateau provides an ideal area to study the responses of grassland ecosystems to anthropogenic activities (Ding et al. 2017). Recent studies emphasize the role of human activities, such as grazing and urbanization, in the degradation of grasslands on the Tibetan Plateau (Tu et al. 2023; Wei et al. 2022). However, the ecological impacts of large infrastructure projects, such as roads and railways, remain poorly understood. Evidence shows that transport infrastructure construction and operation cause vegetation destruction, land-use change, soil erosion, and other ecosystem disruptions (Brtnicky et al. 2022; Feng et al. 2021; Laurance and Balmford 2013). Given the rapid expansion of the transportation network on the Tibetan Plateau in recent years, its disturbance to the ecological environment cannot be ignored.

The Lhasa-Golmud segment of the Tibetan Railway, completed and opened in 2006, spans 1,142 km and is the world's highest and longest plateau railway (Peng et al. 2007). While promoting regional economic development, its construction and operation have also disturbed the grassland ecosystems along the corridor (Brtnicky et al. 2022; Yang, Zhang, and Zhu 2023). Previous studies have reported grassland degradation, reductions in vegetation cover and abundance (Luo et al. 2018; Wang et al. 2015), and elevated local temperatures along the railway (Zhou et al. 2023), which may further impair the carbon sequestration capacity of these ecosystems. However, systematic quantitative assessments of the railway's impact on grassland carbon sequestration remain limited. Additionally, differences in data and methodologies also hinder precise assessment of the extent and intensity of railway-induced disturbances (Ma, Li, and Liu 2021).

This study aims to explore the impact of the Tibetan Railway on the carbon sequestration capacity of grassland ecosystems within the railway corridor. We hypothesize that railway will alter local hydrothermal dynamic with varying distances from grasslands, potentially affecting phenology, photosynthetic capacity, and ultimately annual carbon sequestration. To test this hypothesis, we set the specific objectives: 1) to assess the extent and intensity of railway-induced disturbances on SOS, EOS, and GPPmax; and 2) to quantify the integrated effects of SOS, EOS, and GPPmax on annual GPP within the corridor and elucidate the primary mechanisms through which the railway influences carbon sequestration. This research aims to deepen understanding of railway impacts on plateau ecosystems and carbon cycling, while offering insights for grassland conservation and global green transportation infrastructure development.

## 2. Materials and methods

### 2.1. Study area

The Golmud-Lhasa segment of the Tibetan Railway (Figure 1), spanning from Golmud in Qinghai Province to Lhasa in the Tibet Autonomous Region, was constructed between 2001 and 2006 (Peng et al. 2007). The majority of the railway traverses the flat and expansive terrain of the Tibetan Plateau. The total length of the railway is 1142 km, with altitudes ranging from 2200 m to 5200 m, 84% of which is situated at elevations

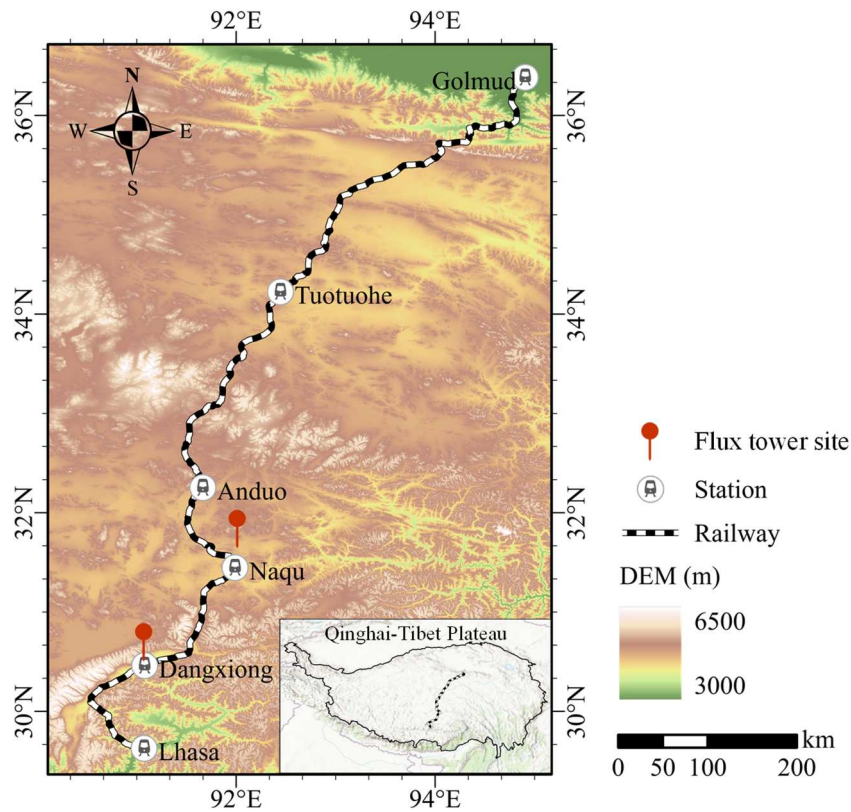


**Figure 1.** Location of the Tibetan Railway (Lhasa-Golmud section), with the background showing the topography of the area along the railway.

above 4000 m. The average annual temperature along the railway ranges from  $-33.6^{\circ}\text{C}$  to  $35.5^{\circ}\text{C}$ , gradually decreasing from southeast to northwest, while the average annual precipitation declines from 500 mm in the southeast to 40 mm in the central region. (Yang, Zhang, and Zhu 2023; Zhou et al. 2023). The primary vegetation types along the railway corridor are alpine meadows and alpine steppes (Karra et al. 2021).

## 2.2. Datasets

### 2.2.1. GPP data from flux towers

GPP data from eddy covariance flux tower measurements were used to establish relationships with remote sensing vegetation indices to estimate regional-scale GPP. Daily GPP data were obtained from two alpine meadow flux tower sites along the Tibetan Railway (see Figure 1): Dangxiong Site ( $30.51^{\circ}\text{N}$ ,  $91.05^{\circ}\text{E}$ ; elevation: 4333 m), recorded observations from 2004 to 2010, with data available from the China Flux Observation and Research Network (<https://www.nesdc.org.cn/>). Naqu Site ( $31.64^{\circ}\text{N}$ ,  $92.01^{\circ}\text{E}$ ; elevation: 4598 m), recorded observations in 2014, 2017, and 2018, with data available from the Big Data Platform for the Pan-Third Pole Environment (<https://poles.tpdc.ac.cn/>) and relevant literature (Wei et al. 2021; Zhang 2022).

### 2.2.2. Satellite data

This study utilized both Sentinel-2 and Landsat data to estimate high-resolution GPP at the regional scale, and Landsat 8 data were used to calculate hydrothermal conditions along the railway.

The Sentinel-2 mission, comprising Sentinel-2A and Sentinel-2B, utilizes multi-spectral instruments to provide high spatial and temporal resolution, capturing 13 spectral bands with spatial resolutions of 10 m (blue, green, red, and near-infrared bands), 20 m (vegetation red-edge, narrow NIR, and SWIR bands), and 60 m (aerosol, water vapor, and SWIR cirrus bands) with a 5-day revisit cycle (Wang et al. 2016). Sentinel-2 Level-2A (L2A) products, pre-processed using the Sen2Cor algorithm and retrieved from the Google Earth

Engine (GEE) platform (Louis et al. 2016), were utilized in this study. Due to the scarcity of continuous Sentinel-2 L2A observational data in the Tibetan Plateau before 2019, all available images from January 1, 2019, to December 31, 2023, were selected. The quality mask band (QA60) was applied to exclude cloud-contaminated and cloud-covered pixels.

Landsat satellites provide the longest temporal record of space-based Earth observations. This study utilized atmospherically corrected Collection 2, Level 2, Tier 1 surface reflectance from Landsat 5, 7, and 8 via GEE. These satellites are equipped with the Thematic Mapper (TM), Enhanced Thematic Mapper Plus (ETM+), and Operational Land Imager (OLI) sensors, respectively (Crawford et al. 2023). Each sensor captures data across visible to shortwave infrared bands at 30 m spatial resolution (15 m for the panchromatic band) and 16-day temporal resolution. Additionally, Landsat 8 is equipped with the Thermal Infrared Sensor, which provides thermal infrared data at 100 m spatial resolution, resampled to 30 meters and aligned with the OLI grid, offering unique support for global medium-resolution land surface temperature monitoring (Vanhellemont 2020). We excluded all Landsat images affected by clouds, cloud shadows, and snow using quality control bands.

### 2.2.3. ESRI landcover

Land use data used in this study were obtained from the ESRI Land Cover project, derived from Sentinel-2 imagery with a 10 m spatial resolution. The dataset provides annual global land cover classifications from 2017 to 2023, generated using Impact Observatory's deep learning model, with an overall accuracy of 85% (Karra et al. 2021). The latest ESRI landcover classification product updates the original 10-class model by merging grassland and scrub into a single rangeland class, which has been widely used in Tibetan Plateau surface classification studies (Ci et al. 2024; Xiao et al. 2024). In this study, only pixels consistently classified as rangeland across all five years (2019–2023) were retained, and the landcover at these pixels is largely consistent with the field sites at Dangxiong and Naqu, supporting the representativeness of the site-based NDGI – GPP relationship along the railway corridor.

## 2.3. Method

### 2.3.1. Estimation of gross primary productivity

We used the satellite-based Normalized Difference Greenness Index (NDGI) as a proxy for GPP and generated a GPP dataset within the Tibetan Railway corridor. NDGI effectively distinguishes vegetation information from soil, snow, and dry grass dynamics (Yang et al. 2019). The calculation formula is as follows:

$$NDGI = \frac{0.65 \times Green + 0.35 \times NIR - Red}{0.65 \times Green + 0.35 \times NIR + Red} \quad (1)$$

where *Red*, *Green*, and *NIR* are the Landsat or Sentinel-2 surface reflectance at the red, green, and near-infrared bands, respectively.

First, due to the temporal mismatch between Sentinel-2 and *in-situ* GPP observations, we utilized Landsat data to extract NDGI and established NDGI-GPP relationships based on the *in-situ* GPP measurements. Previous studies indicate that Landsat 8's narrower spectral bands cause a positive NDGI bias compared to Landsat 5/7 (Roy et al. 2016; Yin et al. 2023). To ensure consistency across datasets, inter-sensor transformation coefficients from Perez and Vitale (2023) were applied to convert Landsat 5/7 bands to the Landsat 8 spectral configuration (Table 1). The coefficients were derived from an Ordinary Least Squares regression between 15,000 Landsat 7 and 8 images, and have been validated for long-term analyses of time series (Perez et al. 2024). The adjusted reflectance were then used to calculate the NDGI. The Landsat-based NDGI at flux sites was calculated as the average value of all pixels within a 300-meter diameter circle centered on the site

**Table 1.** Linear transformation function for matching Landsat 5/7 TM/ETM + to Landsat 8 OLI and Sentinel-2 MSI to Landsat 8 OLI from Perez and Vitale (2023).

Band	Landsat 5/7 TM/ETM + to Landsat 8 OLI	Sentinel-2 MSI to Landsat 8 OLI
Red	OLI = (ETM+/TM + 0.0041)/0.933	OLI = (MSI + 0.0005) / 1.0773
Green	OLI = (ETM+/TM + 0.0037)/0.934	OLI = (MSI - 0.0009) / 1.0518
NIR	OLI = (ETM+/TM - 0.0065)/0.959	OLI = (MSI - 0.10133) / 0.9637

coordinates (Chu et al. 2021). Data pairs with GPP and NDGI values less than 0 were excluded to remove measurement errors and non-vegetative influences, respectively. Least-squares linear regression analysis was then performed using the remaining data pairs to establish NDGI-GPP relationship, with performance evaluated using the coefficient of determination ( $R^2$ ) and root mean square error (RMSE).

Next, we adjusted the 2019–2023 Sentinel-2 reflectance to the Landsat 8 spectral configuration using cross-sensor transformation coefficients from Perez et al. (2024) (Table 1) and calculated the Sentinel-2-based NDGI using the adjusted reflectance.

Finally, the high-resolution GPP was estimated based on the previously established NDGI-GPP relationship and Sentinel-2-based NDGI. For each pixel, GPP values from 2019 to 2023 were calculated and aggregated by day of year (DOY) to generate multi-year averaged seasonal GPP curves, which were further averaged to an 8-day temporal resolution. Annual GPP (GPPann) for each pixel was calculated by summing the GPP values across all 8-day periods and then multiplying the total by 8.

### 2.3.2. Attribution of annual gross primary productivity variation to phenology and physiology

The Statistical Model of Integrated Phenology and Physiology (SMIPP) was employed to analyze the influence of railway on GPPann (Xia et al. 2015; Zhou et al. 2016). The model represents annual carbon fixation as a function of three components, expressed as:

$$GPPann = f(SOS, GPP\ max, EOS) \quad (2)$$

Assuming that SOS, EOS, and GPPmax are independent of one another, the total differential of GPPann can be expressed as:

$$dGPPann = \frac{\partial GPP}{\partial SOS} dSOS + \frac{\partial GPP}{\partial GPP\ max} dGPP\ max + \frac{\partial GPP}{\partial EOS} dEOS \quad (3)$$

where the partial derivatives represent the sensitivity coefficients of the variations in GPPann to the variations in SOS, GPPmax, and EOS, respectively, reflecting the conversion of relative changes in each component to the relative change in GPPann. We use three sensitivity coefficients  $m_{SOS}$ ,  $m_{GPPmax}$  and  $m_{EOS}$  to represent the three partial derivatives. In practice, the relative differences between GPPann and the three indicators can be approximated by the ratio of the anomaly of the variable (i.e. the difference  $\Delta$  between the variable and its value of undisturbed steady state) to the value of undisturbed steady state. In this study, the average value of the variable in the grassland area undisturbed by railways is defined as the undisturbed steady state. Thus, the equation (3) can be transformed to account for each variable's relative contribution:

$$\frac{\Delta GPPann}{GPPann} = m_{SOS} \frac{\Delta SOS}{SOS} + m_{GPP\ max} \frac{\Delta GPP\ max}{GPP\ max} + m_{EOS} \frac{\Delta EOS}{EOS} \quad (4)$$

To facilitate comparison of SOS anomalies with those of EOS, anomalies are conventionally considered positive when SOS advances or EOS is delayed relative to their regional mean values.

The sensitivity coefficients are estimated using multiple linear regression, where  $\Delta GPPann/GPPann$  is the dependent variable, and  $\Delta SOS/SOS$ ,  $\Delta GPP\ max/GPP\ max$  and  $\Delta EOS/EOS$  are the independent variables. The  $R^2$  in multiple linear regression was used to evaluate the applicability of the SMIPP model. Based on the relative changes in each component and their sensitivity coefficients, the independent contributions of SOS, EOS, and GPPmax to the relative variation in GPPann can be quantified. The total sum of these contributions represents the overall relative variation in GPPann.

### 2.3.3. Extraction of phenological and physiological metrics

In Eq. (2), the GPPmax represent the plant physiological properties, while SOS and EOS indicate phenological conditions. We employed the Maximum Separation (MS) method (Descals et al. 2021) to extract SOS and EOS from GPP time series data (Figure S1).

The MS method is a variant of threshold-based techniques that defines a threshold ( $u$ ) using the maximum ( $b_{max}$ ) and minimum ( $b_{min}$ ) of the vegetation index time series, along with the parameter ( $p$ ) (Figure

S1(a)), as follows,

$$u = (b_{\max} - b_{\min})p + b_{\min} \quad (5)$$

where  $p$  was set to 0.5 in this study. Based on threshold ( $u$ ), time series data are binarized to generate a sequence representing the growing season (1) and dormant season (0). A moving window operation is applied to the binarized time series to calculate the difference between the proportion of observations with vegetation activity before and after the central day of the window (Figure S1(b)), as described follows,

$$d = \sum \left( \frac{b'_{\text{before}}}{n_{\text{before}}} - \frac{b'_{\text{after}}}{n_{\text{after}}} \right) \quad (6)$$

where  $n_{\text{before}}$  and  $n_{\text{after}}$  represent the total number of observations before and after the central day of the window, and  $b'_{\text{before}}$  and  $b'_{\text{after}}$  represent the number of observations above the threshold before and after the central day, respectively. Finally, the phenological phases are determined by identifying the extreme values of the proportion difference, with the extreme value close to  $-1$  defining the SOS and the extreme value close to  $1$  defining EOS (Figure S1(c)).

This method requires no complex preprocessing steps, can handle non-smooth time series, and is well-suited for phenological extraction from high-resolution remote sensing data, especially effective when implemented in GEE.

#### 2.3.4. Calculation of hydrothermal condition

The railway may alter hydrothermal conditions along its path, influencing vegetation growth. Therefore, we derive the Land Surface Temperature (LST) and Normalized Difference Moisture Index (NDMI) as proxies for thermal and moisture conditions, respectively. LST was obtained from the Landsat 8 TIR band (Band 10), and subtracting 273.15 converts the temperature from kelvin (K) to celsius ( $^{\circ}\text{C}$ ) (Feng et al. 2021).

NDMI was calculated using the near-infrared (NIR) and shortwave infrared (SWIR) bands from the Landsat OLI sensor, as follows:

$$NDMI = \frac{NIR - SWIR}{NIR + SWIR} \quad (7)$$

NDMI values range from  $-1$  to  $1$ , with higher values indicating greater regional vegetation moisture status (Feng et al. 2021). For each pixel, LST and NDMI from 2019 to 2023 were aggregated by DOY to generate multi-year averaged seasonal climate series curves. We averaged LST and NDMI values over a one-month period before the occurrence of SOS, EOS, and GPPmax to quantify pre-season hydrothermal conditions.

#### 2.3.5. Quantification of the disturbance range and intensity of the Tibetan Railway

To assess the railway's impact on surrounding ecosystems, we conducted a buffer zone analysis. Buffer zones were established perpendicular to the railway centerline at 10-meter intervals, extending up to 500 meters. For each buffer zone, mean values of key ecological indicators (such as SOS, EOS, GPPmax, LST, and NDMI) were calculated for grassland pixels to evaluate variations of each indicator across different buffer zones.

Based on the remarkable segmented trend between the Distance – Ecological Indicators response relationship, a two-piecewise linear regression model was used to determine the disturbance range of the railway, that is, determining the inflection points (Gao et al. 2023). The steps are as follows: ecological indicator data were standardized to a  $[0,1]$  range (Figure S2(a) and (b)). Each point was iteratively evaluated as a candidate inflection point, and piecewise linear regression was performed. Model errors were calculated using the least squares method, and the point with the smallest error value was selected as the optimal inflection point (Figure S2(c)).

Additionally, we analyzed the spatial heterogeneity of the railway's impacts. Specifically, the Tibetan Railway was divided into 114 equal segments of 10 km each. The buffer zone analysis was applied within each section, comparing ecological indicators across buffer zones and the railway centerline. This approach revealed regional variations in disturbance range and intensity.

### 3. Results

#### 3.1. Correlation between in situ GPP measurements and NDGI

Figure 2 (a) and (b) illustrate the GPP time series and corresponding NDGI values at Dangxiong and Naqu sites, respectively. Both NDGI and GPP exhibit a unimodal pattern throughout the year, with NDGI effectively capturing the seasonal dynamics of GPP. The scatterplot in Figure 2(c) demonstrates a strong relationship between NDGI and GPP ( $GPP = 7.23 \times NDGI + 0.232$ , with  $R^2 = 0.79$  and  $RMSE = 0.44$ ). Therefore, NDGI serves as a reliable proxy for estimating GPP and analyzing the carbon dynamics associated with vegetation growth.

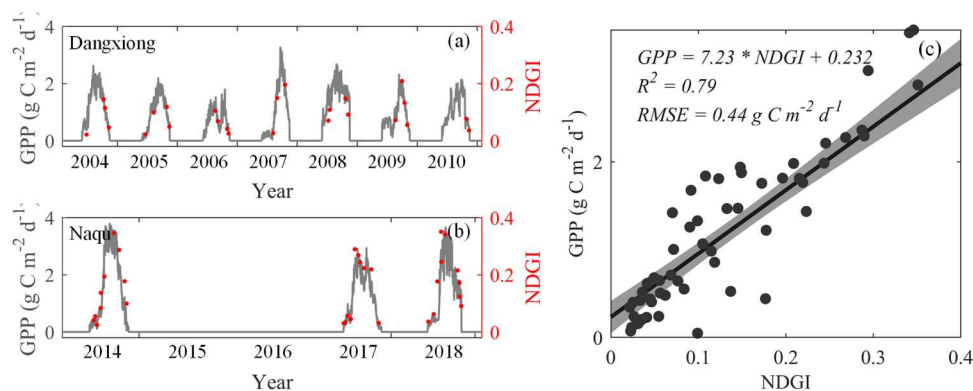
#### 3.2. Variations in phenology and GPPmax within the Tibetan Railway corridor

Figure 3 illustrates the dynamic variations of SOS, EOS, and GPPmax with increasing distance perpendicular to the railway. Within the 500 m buffer zone along the railway, SOS occurs between 160–165 days, EOS between 272–276 days, and GPPmax ranges from 0.9–1.4  $gC\ m^{-2}\ d^{-1}$ . The influence ranges of the Tibetan Railway, indicated by the inflection points, for SOS, EOS, and GPPmax are 40, 50, and 60 m, respectively. Proximity to the railway is associated with earlier SOS (advance rate:  $0.1086\ d\ m^{-1}$ ), delayed EOS (delay rate:  $0.0646\ d\ m^{-1}$ ), and lower GPPmax values (decline rate:  $0.0069\ gC\ m^{-2}\ d^{-1}\ m^{-1}$ ). Overall, the railway primarily impacts the grasslands within a 50-meter range along its route.

Additionally, we analyze the variation of pre-season land surface temperature and moisture with increasing distance perpendicular to the railway (Figure 4). Tibetan Railway causes an increase in pre-season temperature along the corridor, with disturbances primarily concentrated within approximately 80 meters. Temperature change rates for SOS, EOS, and GPPmax pre-season LST were  $-0.0047$ ,  $-0.0042$ , and  $-0.0036\ ^\circ C\ m^{-1}$ , respectively. The railway also leads to a slight reduction in pre-season moisture, with disturbances mainly concentrated within 50 meters. Moisture change rates for SOS, EOS, and GPPmax pre-season NDMI were  $0.0002$ ,  $0.0002$ , and  $0.0005\ m^{-1}$ , respectively.

#### 3.3. Variations in phenology and GPPmax within the Tibetan Railway across different segments

Figure 5 illustrates railway-induced disturbance ranges and intensity for SOS, EOS, and GPPmax across different segments. Specifically, SOS advances by  $\sim 3.5$  days within 20–40 meters (Figure 5(a)), EOS delays by  $\sim 3$  days within 20–50 meters (Figure 5 (b)), and GPPmax decreases by  $0.4\ gC\ m^{-2}\ d^{-1}$  within 30–60 meters (Figure 5(c)). Although the disturbance intensity and range are generally consistent across most segments, slight variations exist in specific sections. For instance, the Lhasa-Dangxiong section (segments 1–15), located near urban zones with significant human activities, shows slight deviations in disturbance intensity and range. The Ando-TuoTuo River section (segments 45–55) and areas near Golmud station



**Figure 2.** Temporal dynamics of in situ GPP and NDGI at (a) Dangxiong and (b) Naqu sites. The gray curve represents GPP, while the red dots indicate NDGI. Note that no GPP data are available for 2015 and 2016 at the Naqu site. (c) Scatterplot of the relationship between GPP and NDGI. The black solid line represents fitted regression line and the gray shading indicates the 95% confidence interval.

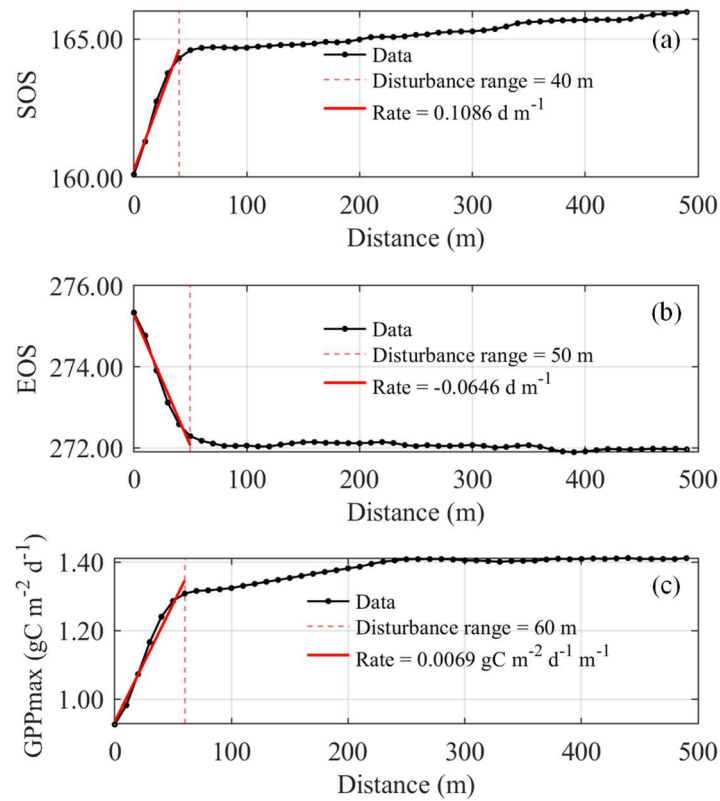


**Figure 3.** Variations in (a) the start of season (SOS), (b) end of season (EOS), and (c) maximum daily GPP during the growing season (GPPmax) within the Tibetan Railway corridor perpendicular to the railway. The vertical red dashed line indicates the disturbance range.

(segments 106–114), dominated by bare soil and sparse vegetation, show no clear disturbance gradient with increasing distance from the railway.

We also analyzed the railway-induced temperature and moisture changes during different seasons, across various sections along its corridor (Figure 6). In most segments, a significant temperature increase was observed within 50 m of the railway center (Figure 6(a)-(c)), indicating higher LST at the railway center

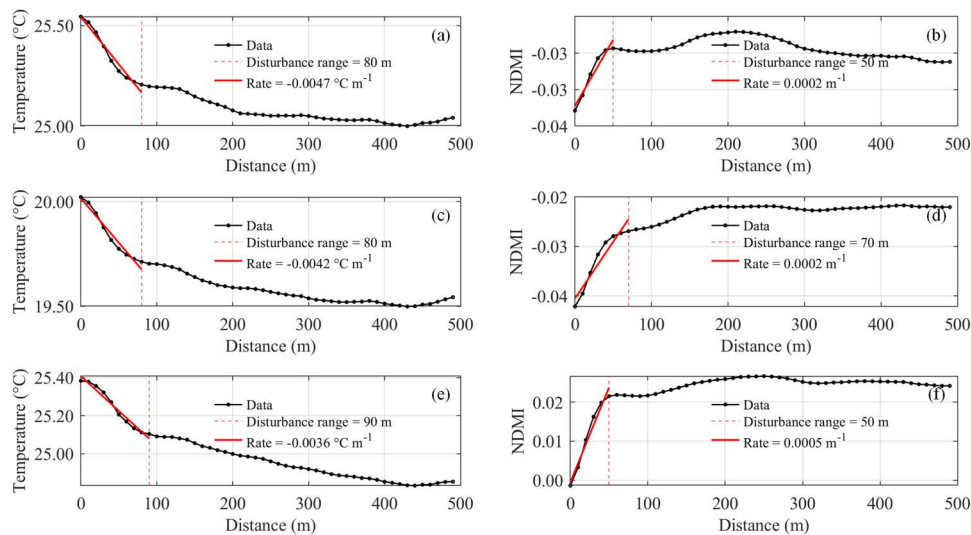


**Figure 4.** Variations in (a) the start of season (SOS), (c) end of season (EOS), and (e) maximum daily GPP during the growing season (GPPmax) pre-season land surface temperature (LST) and (b) in SOS, (d) EOS, and (f) GPPmax pre-season Normalized Difference Moisture Index (NDMI) perpendicular to the railway. The red dashed line indicates the disturbance range.

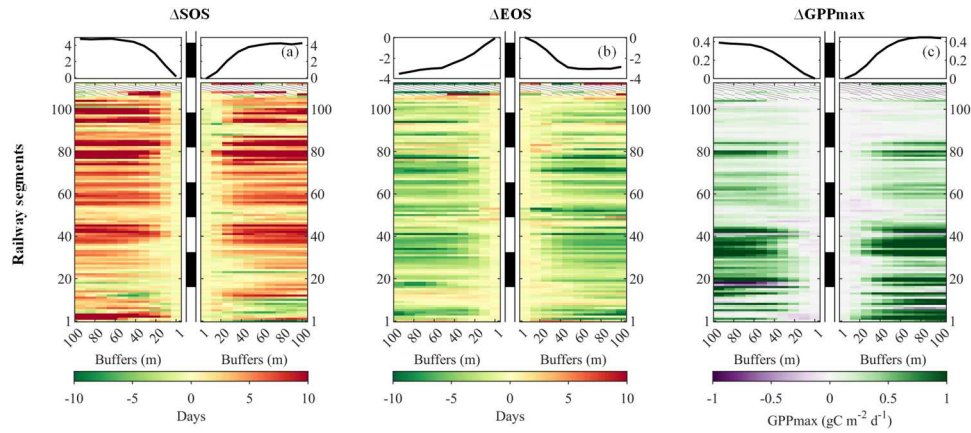


**Figure 5.** Difference ( $\Delta$ ) in (a) the start of season (SOS), (b) end of season (EOS), and (c) maximum daily GPP during the growing season (GPPmax) relative to the railway center across different buffer zones along the Lhasa to Golmud section of the Tibetan Railway which is divided in 114 segments of 10-km long. The curve within the box indicates the variation in the mean difference across different buffer zones.

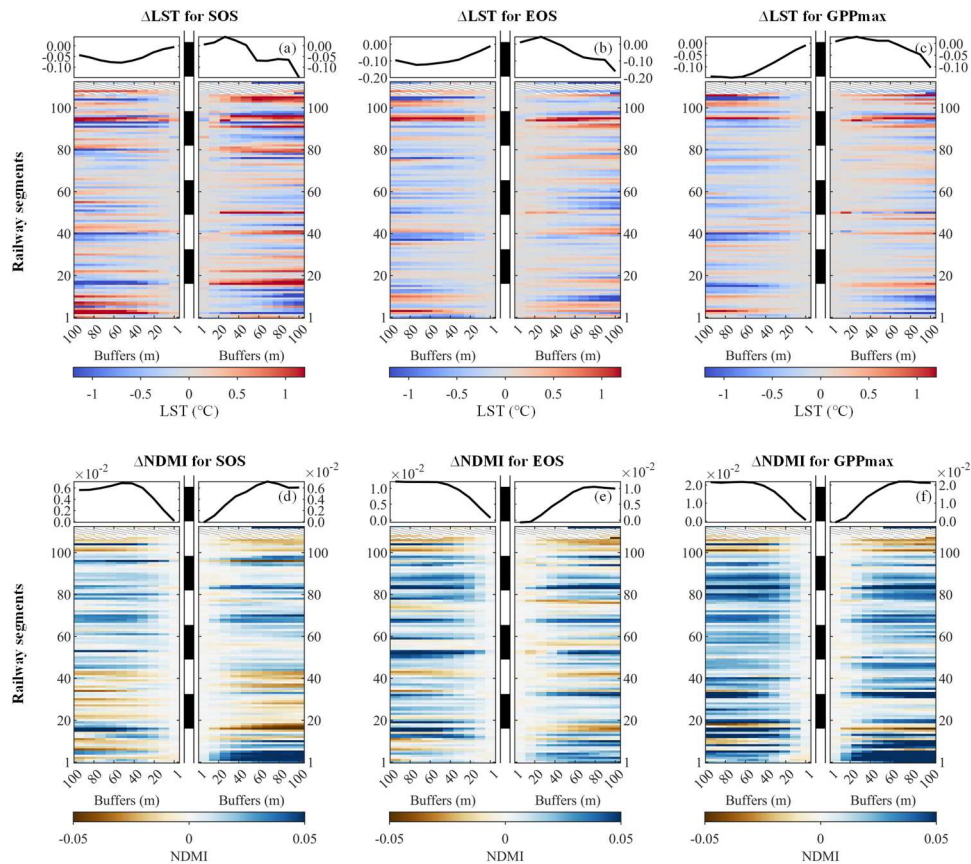


**Figure 6.** Differences ( $\Delta$ ) in (a) the start of season (SOS), (b) end of season (EOS), and (c) maximum daily GPP during the growing season (GPPmax) pre-season land surface temperature (LST), and (d) SOS, (e) EOS, and (f) GPPmax pre-season Normalized Difference Moisture Index (NDMI) relative to the railway center across different buffer zones along the Lhasa to Golmud section of the Tibetan Railway which is divided in 114 segments of 10-km long. The curve within the box indicates the variation in the mean difference across different buffer zones.

compared to surrounding areas. Similarly, the reduction in pre-season moisture was concentrated within 50 m (Figure 6(d)-(f)), reflected by a decline in NDMI values. Beyond 50 m, disturbances in both temperature and moisture gradually stabilized. Overall, temperature and moisture disturbances patterns around SOS, EOS, and

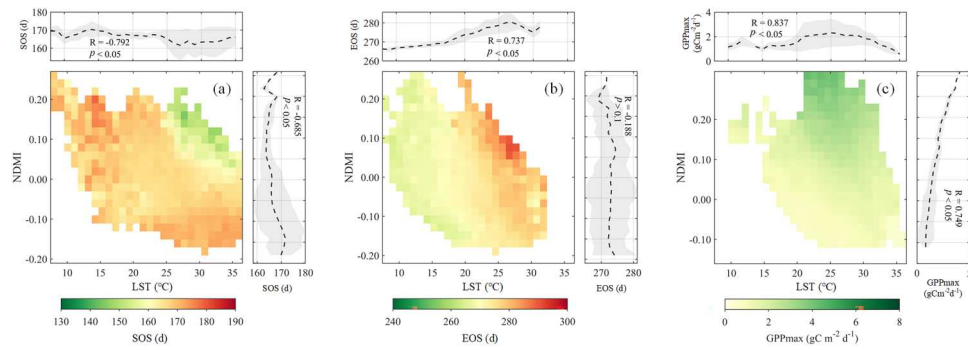


**Figure 7.** Distribution of (a) the start of season (SOS), (b) end of season (EOS), and (c) maximum daily GPP during the growing season (GPPmax) metrics in their respective pre-season hydrothermal space within the 100 m buffer zone of the Qinghai Tibet Railway. The upper box in the figure illustrates the relationship between the metrics and Land Surface Temperature (LST), with metrics averaged over all Normalized Difference Moisture Index (NDMI) bins. The right box in the figure illustrates the relationship between the metrics and NDMI, with metrics averaged over all LST bins.

GPPmax periods were high consistency, however, localized areas exhibited slight deviations, potentially related to site-specific environmental factors such as vegetation cover, soil type, and topographic features.

### 3.4. Variation of phenology and GPPmax with hydrothermal condition

Figure 7 illustrates the distribution patterns of SOS, EOS, and GPPmax in their respective pre-season hydrothermal spaces and their responses to temperature and moisture within the 100 m buffer zone of the Tibetan Railway. SOS is influenced by both temperature and moisture (Figure 7 (a)). Earlier SOS occurrences are closely associated with regions exhibiting relatively higher LST and higher NDMI ( $R = -0.792$ ,  $p < 0.05$ ;  $R = -0.685$ ,  $p < 0.05$ ). EOS is primarily controlled by temperature (Figure 7 (b)), with significant delay in areas with higher temperatures ( $R = 0.737$ ,  $p < 0.05$ ). Moisture has no significant effect on EOS ( $p > 0.1$ ). GPPmax is influenced by both temperature and moisture, exhibiting a clear nonlinear pattern in the LST space (Figure 7 (c)). The highest GPPmax occurs in regions with temperatures around 25°C and relatively higher moisture levels. In regions where temperatures deviate from 25°C, GPPmax values significantly decline ( $R = 0.837$ ,  $p < 0.05$ ). Additionally, moisture has a significant positive effect on GPPmax ( $R = 0.749$ ,  $p < 0.05$ ).

### 3.5. Estimation of GPPmax variation caused by Tibetan Railway

We calculated relative anomalies within the 100 m buffer zone along the railway and established a multiple regression model to estimate phenological and physiological sensitivity coefficients in the SMIPP model. The regression results indicated sensitivity coefficients of  $m_{\text{SOS}} = 0.2164$ ,  $m_{\text{GPPmax}} = 1.2211$ , and  $m_{\text{EOS}} = 1.2209$ . Together, the three indicators accounted for 94.64% of the variation in annual GPP, with the regression equation being statistically significant at the 0.01 level (Figure S3), demonstrating that the SMIPP model effectively explains the variability in GPPann.

The contributions of each indicator to GPPann variation were calculated by multiplying their relative anomalies, sensitivity coefficients, and mean annual GPP (see Eq. (4)). Tibetan Railway increased GPPann by approximately 28.82 MgC  $\text{y}^{-1}$  through advancing SOS and by 104.26 MgC  $\text{y}^{-1}$  through delaying EOS. In contrast, railway's influence on GPPmax resulted in a carbon reduction of approximately 2952.79 MgC  $\text{y}^{-1}$ . Overall, the trade-off between Tibetan Railway influences on phenology and physiology leads to a net carbon loss of approximately 2819.71 MgC  $\text{y}^{-1}$  (Figure 8).

## 4. Discussion

### 4.1. Disturbance range and intensity of Tibetan Railway on grassland activity

Identifying railway-induced disturbance range and intensity is crucial for prioritizing key regions for ecological protection. Previous studies using low-resolution remote sensing data or large buffer zones have

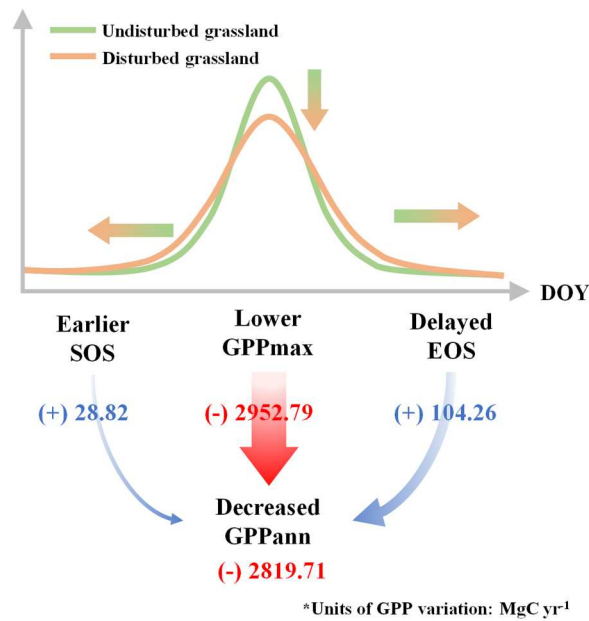


**Figure 8.** Schematic diagram of the impact of the Tibetan Railway on annual cumulative GPP (GPPann). The Tibetan Railway affects GPPann through vegetation phenology (the start and end of season i.e. SOS and EOS) and physiology (maximum GPP during the growing season i.e. GPPmax). The blue and red arrows represent the increase and decrease in GPP, respectively. The values adjacent to the arrows indicate the specific changes in GPP.

indicated that railway impact distance can span several hundred meters to kilometers (Feng et al. 2021; Ma, Li, and Liu 2021). However, such low-resolution datasets often fail to accurately capture localized ecological changes and may misattribute elevation-driven or slope-driven impacts to railway disturbances. In the Tibetan Plateau, phenology shifts by  $\sim 0.8$ – $1.1$  days per 100 m elevation increase (Shen et al. 2022). Our analysis of elevation variations (Figure S4) shows that within 100 m of the railway, only 8.23% of pixels had elevation differences exceeding 10 m, decreasing to 4.25% within 50 m. Slope analysis (Figure S5) indicates that over 99% of the area within 100 m of the railway has slope differences less than  $5^\circ$ , effectively approaching flat terrain. Moreover, Mann – Whitney U tests show no significant differences between railway center pixels and surrounding buffer pixels in elevation ( $p = 0.9871$ ) or slope ( $p = 0.8516$ ). Given such minimal topographic variation, the observed changes in phenology and GPPmax in this study are more likely attributable to railway-induced disturbances rather than terrain effects.

The disturbance range derived from high-resolution data (Sentinel-2 and Landsat) in this study ( $\sim 50$  m) is much smaller than the disturbance zone obtained from low-resolution data (GIMMS or MODIS), and aligns with several field-based measurements. For example, Chen, Li, and Zhang (2003) reported significant vegetation biomass reduction within a 50-meter buffer zone due to railway construction. Similarly, Deljouei et al. (2018) reported road-caused significant changes in soil properties, forest structure, and vegetation composition within 30 meters of their edges.

This study underscores the superiority of open-accessed decametric-scale remote sensing data over hectometric or kilometric data for road ecology studies, and calls for a reexamine of similar studies rely on low resolution remote sensing data (Feng et al. 2021; Ma, Li, and Liu 2021). Additionally, it is worth noting that, although the Tibetan Railway's disturbance range on the ecosystem is relatively small, its long length means that the impact should not be overlooked.

#### 4.2. Impacts of the Tibetan Railway on phenology and physiology

This study reveals that Tibetan Railway has altered grassland phenology and photosynthesis, leading to earlier SOS, delayed EOS, and significantly reduced GPPmax within its vicinity. The mechanisms underlying these changes can be attributed to alterations in hydrothermal conditions caused by the railway, which subsequently affect plant phenology and photosynthetic capacity.

The railway significantly altered the local hydrothermal condition within a 50-meter buffer zone, increasing surface temperatures and reducing soil moisture (Figure 4), with consistent disturbance patterns observed in spring (SOS), summer (time of  $GPP_{max}$ ), and autumn (EOS). The reduction in vegetation cover due to railway, driven by vegetation removal (Laurance and Balmford 2013) and chemical pollution (Brtnicky et al. 2022), led to greater solar radiation absorption on exposed surfaces (Migała et al. 2014) and less heat dissipation via evapotranspiration (Kunert et al. 2015), thereby substantially increasing surface temperature. Moreover, vegetation loss weakened the soil water retention, increased surface runoff, and reduced water recycling, further exacerbating soil moisture loss (Domec et al. 2010; Nadezhkina et al. 2009). These findings align with previous studies, such as Feng et al. (2021), which reported that vegetation removal intensified arid and warm surface conditions, and Nedbal and Brom (2018), who observed temperature increases of up to 7°C due to road-induced vegetation loss and water depletion.

The railway-induced changes in temperature and soil moisture played crucial roles in regulating plant phenology and photosynthetic capacity. Elevated temperatures within the railway corridor were primary drivers for the earlier SOS and delayed EOS (Figure 7). Warmer spring temperatures accelerated thermal accumulation, enabling plants to meet thermal requirements faster and advancing SOS (Chen et al. 2023). Similarly, elevated autumn temperatures enhance photosynthetic enzyme activity, delaying chlorophyll degradation and leaf senescence, ultimately causing a later EOS (Li et al. 2023; Wang et al. 2024). For  $GPP_{max}$ , moderate increases in temperature can enhance photosynthetic efficiency, but temperatures exceeding optimal ranges can inhibit photosynthesis, particularly under water stress conditions (Huang et al. 2019).

Reduced soil moisture within the railway corridor also influenced SOS, EOS, and  $GPP_{max}$  (Figure 7). For SOS, decreased soil moisture slowed water absorption by roots, delaying phenological onset (Ge et al. 2021). In contrast, EOS was less affected by soil moisture depletion, as plants in autumn are in a senescent state with lower water requirements (Yu et al. 2022), consistent with the lack of significant effects observed in this study. Soil moisture depletion had a more pronounced impact on  $GPP_{max}$ , under high-temperature conditions, reduced soil moisture intensified plant transpiration, exacerbating water stress and significantly limiting  $GPP_{max}$  (Chen et al. 2021).

#### 4.3. Contribution of variations in phenology and physiology to annual GPP

The railway-induced advancement of SOS and delay of EOS significantly extended the growing season of alpine grassland ecosystems, thereby contributing positively to carbon sequestration. The extended growing season provided plants with more time for photosynthesis, increasing the annual cumulative carbon uptake (Grossiord et al. 2022). Previous studies have shown that each additional day of growing season length can increase GPP by approximately  $5.8 \text{ gC m}^{-2} \text{ y}^{-1}$  (Piao et al. 2007), consistent with the observed trend of enhanced carbon sequestration resulting from a prolonged growing season in this study.

However, the negative impact of the railway on  $GPP_{max}$  was the primary drivers of net carbon loss, overshadowing the positive effects of SOS and EOS.  $GPP_{max}$  reflects the peak photosynthetic capacity of plants during the growing season and is critical for regulating carbon uptake efficiency throughout the season (Hu et al. 2018). Previous studies support this finding, with Xia et al. (2015) and Zhang et al. (2022) demonstrating that  $GPP_{max}$  contributes more to  $GPP_{ann}$  than growing season length in Northern Hemisphere grasslands. Similarly, Hu et al. (2018) found that in 87% of ecosystems,  $GPP_{max}$  had a more significant role in determining  $GPP_{ann}$  than growing season length, which only significantly correlated with  $GPP_{ann}$  in 10% of ecosystems. Therefore, although the changes in SOS and EOS due to railway partially mitigate carbon losses, the predominant role of  $GPP_{max}$  reductions ultimately leads to decreased carbon sequestration along the railway corridor.

Annual carbon sequestration on the Tibetan Plateau is approximately  $713.0 \pm 81.6 \text{ TgC y}^{-1}$  (Wei et al. 2021). This study reveals that the carbon loss attributed to railway disturbances amounts to  $2819.71 \text{ MgC y}^{-1}$ , accounting for approximately 0.0035%–0.0045% of the plateau's annual carbon sequestration. Although this proportion is relatively small, its impact is long-term along the 1142 km railway corridor. In recent years, as transportation infrastructure expands across the Tibetan Plateau, it increasingly disrupts alpine grassland ecosystems (Gao and Li 2022). This study quantifies the impact of infrastructure disturbances on carbon cycles on the Tibetan Plateau and provides insights for assessing the effects of global linear

infrastructure on carbon balance, aiding policy development to balance ecological protection with infrastructure growth. For existing railways, ecological restoration should focus on the 100 m corridor along the line, including measures such as fence closure and grazing prohibition (Wu et al. 2010), grass seed replanting (Zhou et al. 2023) and fertilization (Song and Yu 2015), thereby mitigating the negative impacts of railways on ecosystems and enhancing carbon sequestration along the corridor.

#### **4.4. Research limitations and future prospects**

This study systematically explored the impact of the Tibetan Railway on the carbon sink function of alpine grassland ecosystems. However, several limitations should be addressed to enhance the broader applicability and practical significance of the findings.

First, due to the limited availability of Sentinel data in the Tibetan Plateau, the time span of the data used in this study (2019–2023) is relatively short. This period captures the recent impacts of the railway but does not allow a comprehensive assessment of additional disturbance effects. Future work should integrate longer-term datasets to facilitate this evaluation. Second, the NDGI – GPP relationship in this study was established solely from field data at Dangxiong and Naqu, and future studies should incorporate additional field observations along the railway to enhance the accuracy and reliability of GPP estimates. Third, this study primarily focused on the impacts of railways on carbon sequestration through microclimate alterations, while other potential mechanisms of disturbance caused by the railway – such as changes in soil structure, land cover change and other vegetation management practices by the railway, were less considered. Future research can investigate these additional disturbance mechanisms to provide a more holistic understanding of railway impacts on carbon dynamics in sensitive ecosystems. Finally, the impact of railway disturbances on carbon sequestration can vary across regions and ecosystem types, and there is currently a lack of global-scale studies to quantify their effects on carbon balance. Future research should focus on regional comparisons and global-scale assessments to accurately quantify carbon losses associated to infrastructure development, thereby providing a solid scientific basis for global carbon budget evaluations.

## **5. Conclusion**

This study reveals the impact of the Tibetan Railway on the phenology and GPPmax of grassland ecosystems, further assessing the railway's effect on GPPann sequestration using SMIPP model. The results indicate that Tibetan Railway significantly impacts phenology and GPPmax within a 50-meter range, manifested as earlier SOS, delayed EOS, and reductions in GPPmax. These phenomena are primarily attributed to the microclimate changes induced by the railway, which render the corridor drier and hotter compared to the surrounding background climate.

The analysis via the SMIPP model indicates that Tibetan Railway increased ecosystem GPPann by 28.82 MgC y<sup>-1</sup> and 104.26 MgC y<sup>-1</sup> due to its effects on SOS and EOS, respectively. However, a decrease in GPPann of 2952.79 MgC y<sup>-1</sup> resulted from its impact on GPPmax. Although earlier SOS and delayed EOS extended the growing season and promoted carbon accumulation, the decline in GPPmax was the primary driver of reduced carbon sequestration, ultimately resulting in a net annual carbon loss along the railway corridor. This study provides scientific evidence for evaluating the carbon sequestration function of grassland ecosystems along the Tibetan Railway and highlights the importance of considering ecological impacts in infrastructure planning.

## **Disclosure statement**

No potential conflict of interest was reported by the author(s).

## **Funding**

This work was supported by the Xizang Science and Technology Major Program [grant number XZ202402ZD0003-09]; the National Natural Science Foundation of China [grant numbers 42271323]; and the National Key Research and Development Program of China [grant number 2023YFF1303602].

## CRediT authorship contribution statement

**Yajie Yang:** Conceptualization, Data curation, Formal analysis, Investigation, Software, Visualization, Writing – Original draft, Writing – Review & editing. **Gaofei Yin:** Conceptualization, Funding acquisition, Investigation, Methodology, Project administration, Resources, Supervision, Validation, Writing – Original draft, Writing – Review & editing. **Jiangliu Xie** and **Rui Chen:** Visualization, Writing – Review & editing. **Dujuan Ma** and **Changjing Wang:** Data curation, Writing – Review & editing. **Lu Zhou:** Resources, Funding acquisition. **Lin Huang:** Resources, Data curation. **Guodong Zhang, Meilian Wang, Qiaoyun Xie, Aleixandre Verger, Adrià Descals, Iolanda Filella** and **Josep Peñuelas:** Writing – Review & editing.

## Data availability statement

The data that support the findings of this study are available from the corresponding author upon request.

## ORCID

Adrià Descals  <https://orcid.org/0000-0003-1644-3036>

## References

- Anav, A., P. Friedlingstein, C. Beer, P. Ciais, A. Harper, C. Jones, G. Murray-Tortarolo, et al. 2015. “Spatiotemporal Patterns of Terrestrial Gross Primary Production: A Review.” *Reviews of Geophysics* 53 (3): 785–818. <https://doi.org/10.1002/2015rg000483>.
- Beer, C., M. Reichstein, E. Tomelleri, P. Ciais, M. Jung, N. Carvalhais, C. Rödenbeck, et al. 2010. “Terrestrial Gross Carbon Dioxide Uptake: Global Distribution and Covariation with Climate.” *Science* 329 (5993): 834–838. <https://doi.org/10.1126/science.1184984>.
- Brtnicky, M., V. Pecina, D. Juricka, P. Kowal, M. Vasinova Galiova, T. Baltazar, and M. Radziemska. 2022. “Can Rail Transport-Related Contamination Affect Railway Vegetation? A Case Study of a Busy Railway Corridor in Poland.” *Chemosphere* 293:133521. <https://doi.org/10.1016/j.chemosphere.2022.133521>.
- Chen, H., S. Li, and Y. Zhang. 2003. “Impact of Road Construction on Vegetation alongside Qinghai-Xizang Highway and Railway.” *Chinese Geographical Science* 13 (4): 340–346. <https://doi.org/10.1007/s11769-003-0040-5>.
- Chen, N., C. Song, X. Xu, X. Wang, N. Cong, P. Jiang, J. Zu, et al. 2021. “Divergent Impacts of Atmospheric Water Demand on Gross Primary Productivity in Three Typical Ecosystems in China.” *Agricultural and Forest Meteorology* 307:108527. <https://doi.org/10.1016/j.agrformet.2021.108527>.
- Chen, Z., R. Chen, Y. Yang, H. Pan, Q. Xie, C. Wang, B. Xu, and G. Yin. 2023. “Decreased Sensitivity of Grassland Spring Phenology to Temperature on the Tibetan Plateau.” *IEEE Journal of Selected Topics in Applied Earth Observations and Remote Sensing* 16:4371–4382. <https://doi.org/10.1109/jstars.2023.3269908>.
- Chu, H., X. Luo, Z. Ouyang, W. S. Chan, S. Dengel, S. C. Biraud, M. S. Torn, et al. 2021. “Representativeness of Eddy-Covariance Flux Footprints for Areas Surrounding AmeriFlux Sites.” *Agricultural and Forest Meteorology* 301:108350. <https://doi.org/10.1016/j.agrformet.2021.108350>.
- Ci, M., Q. Liu, Y. Liu, Q. Jin, J. Martinez-Valderrama, and J. Zhao. 2024. “Multi-model Assessment of Potential Natural Vegetation to Support Ecological Restoration.” *Journal of Environmental Management* 367:121934. <https://doi.org/10.1016/j.jenvman.2024.121934>.
- Cong, N., M. Shen, W. Yang, Z. Yang, G. Zhang, and S. Piao. 2017. “Varying Responses of Vegetation Activity to Climate Changes on the Tibetan Plateau Grassland.” *International Journal of Biometeorology* 61 (8): 1433–1444. <https://doi.org/10.1007/s00484-017-1321-5>.
- Crawford, C. J., D. P. Roy, S. Arab, C. Barnes, E. Vermote, G. Hulley, A. Gerace, et al. 2023. “The 50-Year Landsat Collection 2 Archive.” *Science of Remote Sensing* 61 (8): 831–842. <https://doi.org/10.1016/j.srs.2023.100103>.
- Deljouei, A., S. M. M. Sadeghi, E. Abdi, M. Bernhardt-Römermann, E. L. Pascoe, and M. Marcantonio. 2018. “The Impact of Road Disturbance on Vegetation and Soil Properties in a Beech Stand, Hyrcanian Forest.” *European Journal of Forest Research* 137 (6): 759–770. <https://doi.org/10.1007/s10342-018-1138-8>.
- Deng, Y., X. Wang, K. Wang, P. Ciais, S. Tang, L. Jin, L. Li, and S. Piao. 2021. “Responses of Vegetation Greenness and Carbon Cycle to Extreme Droughts in China.” *Agricultural and Forest Meteorology* 298–299:108307. <https://doi.org/10.1016/j.agrformet.2020.108307>.
- Descals, A., A. Verger, G. Yin, and J. Penuelas. 2021. “A Threshold Method for Robust and Fast Estimation of Land-Surface Phenology Using Google Earth Engine.” *IEEE Journal of Selected Topics in Applied Earth Observations and Remote Sensing* 14:601–606. <https://doi.org/10.1109/jstars.2020.3039554>.
- Ding, J., L. Chen, C. Ji, G. Hugelius, Y. Li, L. Liu, S. Qin, et al. 2017. “Decadal Soil Carbon Accumulation across Tibetan Permafrost Regions.” *Nature Geoscience* 10 (6): 420–424. <https://doi.org/10.1038/ngeo2945>.
- Domec, J. C., J. S. King, A. Noormets, E. Treasure, M. J. Gavazzi, G. Sun, and S. G. McNulty. 2010. “Hydraulic Redistribution of Soil Water by Roots Affects Whole-Stand Evapotranspiration and net Ecosystem Carbon Exchange.” *New Phytologist* 187 (1): 171–183. <https://doi.org/10.1111/j.1469-8137.2010.03245.x>.

- Fang, Z., W. Zhang, L. Wang, G. Schurgers, P. Ciais, J. Peñuelas, M. Brandt, et al. 2024. "Global Increase in the Optimal Temperature for the Productivity of Terrestrial Ecosystems." *Communications Earth & Environment* 5 (1). <https://doi.org/10.1038/s43247-024-01636-9>.
- Feng, S., S. Liu, L. Jing, Y. Zhu, W. Yan, B. Jiang, M. Liu, et al. 2021. "Quantification of the Environmental Impacts of Highway Construction Using Remote Sensing Approach." *Remote Sensing* 13 (7): 1340. <https://doi.org/10.3390/rs13071340>.
- Gao, D., and S. Li. 2022. "Spatiotemporal Impact of Railway Network in the Qinghai-Tibet Plateau on Accessibility and Economic Linkages during 1984–2030." *Journal of Transport Geography* 100:103332. <https://doi.org/10.1016/j.jtrangeo.2022.103332>.
- Gao, S., R. Zhong, K. Yan, X. Ma, X. Chen, J. Pu, S. Gao, J. Qi, G. Yin, and R. B. Myneni. 2023. "Evaluating the Saturation Effect of Vegetation Indices in Forests Using 3D Radiative Transfer Simulations and Satellite Observations." *Remote Sensing of Environment* 295:113665. <https://doi.org/10.1016/j.rse.2023.113665>.
- Ge, W., J. Han, D. Zhang, and F. Wang. 2021. "Divergent Impacts of Droughts on Vegetation Phenology and Productivity in the Yungui Plateau, Southwest China." *Ecological Indicators* 127:107743. <https://doi.org/10.1016/j.ecolind.2021.107743>.
- Grossiord, C., C. Bachofen, J. Gisler, E. Mas, Y. Vitasse, and M. Didion-Gency. 2022. "Warming May Extend Tree Growing Seasons and Compensate for Reduced Carbon Uptake during dry Periods." *Journal of Ecology* 110 (7): 1575–1589. <https://doi.org/10.1111/1365-2745.13892>.
- Hu, Z., H. Shi, K. Cheng, Y. Wang, S. Piao, Y. Li, L. Zhang, et al. 2018. "Joint Structural and Physiological Control on the Interannual Variation in Productivity in a Temperate Grassland: A Data-Model Comparison." *Global Change Biology* 24 (7): 2965–2979. <https://doi.org/10.1111/gcb.14274>.
- Huang, M., S. Piao, P. Ciais, J. Penuelas, X. Wang, T. F. Keenan, S. Peng, et al. 2019. "Air Temperature Optima of Vegetation Productivity across Global Biomes." *Nature Ecology & Evolution* 3 (5): 772–779. <https://doi.org/10.1038/s41559-019-0838-x>.
- Karra, K., C. Kontgis, Z. Statman-Weil, J. C. Mazzariello, M. Mathis, and S. P. Brumby. 2021. "Global Land use / Land Cover with Sentinel 2 and Deep Learning." 2021 IEEE International Geoscience and Remote Sensing Symposium IGARSS, 4704–4707. <https://doi.org/10.1109/igarss47720.2021.9553499>.
- Keenan, T. F., J. Gray, M. A. Friedl, M. Toomey, G. Bohrer, D. Y. Hollinger, J. W. Munger, et al. 2014. "Net Carbon Uptake Has Increased through Warming-Induced Changes in Temperate Forest Phenology." *Nature Climate Change* 4 (7): 598–604. <https://doi.org/10.1038/nclimate2253>.
- Kunert, N., L. M. T. Aparecido, N. Higuchi, J. d. Santos, and S. Trumbore. 2015. "Higher Tree Transpiration due to Road-Associated Edge Effects in a Tropical Moist Lowland Forest." *Agricultural and Forest Meteorology* 213:183–192. <https://doi.org/10.1016/j.agrformet.2015.06.009>.
- Laurance, W. F., and A. Balmford. 2013. "A Global map for Road Building." *Nature* 495 (7441): 308–309. <https://doi.org/10.1038/495308a>.
- Li, W., R. Chen, D. Ma, C. Wang, Y. Yang, C. Wang, H. Chen, and G. Yin. 2023. "Tracking Autumn Photosynthetic Phenology on Tibetan Plateau Grassland with the Green – red Vegetation Index." *Agricultural and Forest Meteorology* 339:109573. <https://doi.org/10.1016/j.agrformet.2023.109573>.
- Louis, J., V. Debaecker, B. Pflug, M. Main-Knorn, J. Bieniarz, U. Mueller-Wilm, E. Cadau, and F. Gascon. 2016. "SENTINEL-2 SEN2COR: L2a Processor for Users." Paper presented at the Proceedings Living Planet Symposium 2016, Prague, Czech Republic, May 2016.
- Luo, L., W. Ma, Y. Zhuang, Y. Zhang, S. Yi, J. Xu, Y. Long, D. Ma, and Z. Zhang. 2018. "The Impacts of Climate Change and Human Activities on Alpine Vegetation and Permafrost in the Qinghai-Tibet Engineering Corridor." *Ecological Indicators* 93:24–35. <https://doi.org/10.1016/j.ecolind.2018.04.067>.
- Ma, C., T. Li, and P. Liu. 2021. "GIMMS NDVI3g+ (1982-2015) Response to Climate Change and Engineering Activities along the Qinghai – Tibet Railway." *Ecological Indicators* 128:107821. <https://doi.org/10.1016/j.ecolind.2021.107821>.
- Miłała, K., B. Wojtuń, W. Szymański, and P. Muskała. 2014. "Soil Moisture and Temperature Variation under Different Types of Tundra Vegetation during the Growing Season: A Case Study from the Fuglebekken Catchment, SW Spitsbergen." *Catena* 116:10–18. <https://doi.org/10.1016/j.catena.2013.12.007>.
- Nadezhdina, N., K. Steppe, D. J. De Pauw, R. Bequet, J. Cermak, and R. Ceulemans. 2009. "Stem-mediated Hydraulic Redistribution in Large Roots on Opposing Sides of a Douglas-fir Tree Following Localized Irrigation." *New Phytologist* 184 (4): 932–943. <https://doi.org/10.1111/j.1469-8137.2009.03024.x>.
- Nedbal, V., and J. Brom. 2018. "Impact of Highway Construction on Land Surface Energy Balance and Local Climate Derived from LANDSAT Satellite Data." *Science of the Total Environment* 633:658–667. <https://doi.org/10.1016/j.scitotenv.2018.03.220>.
- Peng, C., H. Ouyang, Q. Gao, Y. Jiang, F. Zhang, J. Li, and Q. Yu. 2007. "Building a "Green" Railway in China." *Science* 316 (5824): 546–547. <https://doi.org/10.1126/science.1134134>.
- Perez, M., D. Lombardi, G. Bardino, and M. Vitale. 2024. "Drought Assessment through Actual Evapotranspiration in Mediterranean Vegetation Dynamics." *Ecological Indicators* 166:112359. <https://doi.org/10.1016/j.ecolind.2024.112359>.
- Perez, M., and M. Vitale. 2023. "Landsat-7 ETM+, Landsat-8 OLI, and Sentinel-2 MSI Surface Reflectance Cross-Comparison and Harmonization over the Mediterranean Basin Area." *Remote Sensing* 15 (16): 4008. <https://doi.org/10.3390/rs15164008>.

- Piao, S., J. Fang, P. Ciais, P. Peylin, Y. Huang, S. Sitch, and T. Wang. 2009. "The Carbon Balance of Terrestrial Ecosystems in China." *Nature* 458 (7241): 1009–1014. <https://doi.org/10.1038/nature07944>.
- Piao, S., P. Friedlingstein, P. Ciais, N. Viovy, and J. Demarty. 2007. "Growing Season Extension and Its Impact on Terrestrial Carbon Cycle in the Northern Hemisphere over the Past 2 Decades." *Global Biogeochemical Cycles* 21 (3). <https://doi.org/10.1029/2006gb002888>.
- Roy, D. P., V. Kovalskyy, H. K. Zhang, E. F. Vermote, L. Yan, S. S. Kumar, and A. Egorov. 2016. "Characterization of Landsat-7 to Landsat-8 Reflective Wavelength and Normalized Difference Vegetation Index Continuity." *Remote Sensing of Environment* 185 (1): 57–70. <https://doi.org/10.1016/j.rse.2015.12.024>.
- Running, S. W. 2008. "Ecosystem Disturbance, Carbon, and Climate." *Science* 321 (5889): 652–653. <https://doi.org/10.1126/science.1159607>.
- Shen, M., S. Wang, N. Jiang, J. Sun, R. Cao, X. Ling, B. Fang, et al. 2022. "Plant Phenology Changes and Drivers on the Qinghai – Tibetan Plateau." *Nature Reviews Earth & Environment* 3 (10): 633–651. <https://doi.org/10.1038/s43017-022-00317-5>.
- Song, M. H., and F. H. Yu. 2015. "Reduced Compensatory Effects Explain the Nitrogen-Mediated Reduction in Stability of an Alpine Meadow on the Tibetan Plateau." *New Phytologist* 207 (1): 70–77. <https://doi.org/10.1111/nph.13329>.
- Stoy, P. C., A. M. Trowbridge, and W. L. Bauerle. 2014. "Controls on Seasonal Patterns of Maximum Ecosystem Carbon Uptake and Canopy-Scale Photosynthetic Light Response: Contributions from Both Temperature and Photoperiod." *Photosynthesis Research* 119 (1-2): 49–64. <https://doi.org/10.1007/s11120-013-9799-0>.
- Tu, W., Y. Du, J. Yi, F. Liang, N. Wang, J. Qian, S. Huang, P. Luo, and X. Wang. 2023. "Assessment of the Dynamic Ecological Networks on the Qinghai-Tibet Plateau Using Human's Digital Footprints." *Ecological Indicators* 147:109954. <https://doi.org/10.1016/j.ecolind.2023.109954>.
- Vanhellemont, Q. 2020. "Combined Land Surface Emissivity and Temperature Estimation from Landsat 8 OLI and TIRS." *ISPRS Journal of Photogrammetry and Remote Sensing* 166:390–402. <https://doi.org/10.1016/j.isprsjprs.2020.06.007>.
- Wang, C., Y. Yang, G. Yin, Q. Xie, B. Xu, A. Verger, A. Descals, I. Filella, and J. Peñuelas. 2024. "Divergence in Autumn Phenology Extracted from Different Satellite Proxies Reveals the Timetable of Leaf Senescence over Deciduous Forests." *Geophysical Research Letters* 51 (4). <https://doi.org/10.1029/2023gl107346>.
- Wang, G., A. R. Gillespie, S. Liang, A. Mushkin, and Q. Wu. 2015. "Effect of the Qinghai – Tibet Railway on Vegetation Abundance." *International Journal of Remote Sensing* 36 (19-20): 5222–5238. <https://doi.org/10.1080/01431161.2015.1041179>.
- Wang, Q., W. Shi, Z. Li, and P. M. Atkinson. 2016. "Fusion of Sentinel-2 Images." *Remote Sensing of Environment* 187:241–252. <https://doi.org/10.1016/j.rse.2016.10.030>.
- Wang, Y., W. Lv, K. Xue, S. Wang, L. Zhang, R. Hu, H. Zeng, X. Xu, Y. Li, and L. Jiang. 2022. "Grassland Changes and Adaptive Management on the Qinghai – Tibetan Plateau." *Nature Reviews Earth & Environment* 3 (10): 668–683. <https://doi.org/10.1038/s43017-022-00330-8>.
- Wei, D., Y. Qi, Y. Ma, X. Wang, W. Ma, T. Gao, L. Huang, H. Zhao, J. Zhang, and X. Wang. 2021. "Plant Uptake of CO<sub>2</sub> Outpaces Losses from Permafrost and Plant Respiration on the Tibetan Plateau." *Proceedings of the National Academy of Sciences of the United States of America* 118 (33). <https://doi.org/10.1073/pnas.2015283118>.
- Wei, Y., H. Lu, J. Wang, X. Wang, and J. Sun. 2022. "Dual Influence of Climate Change and Anthropogenic Activities on the Spatiotemporal Vegetation Dynamics over the Qinghai-Tibetan Plateau from 1981 to 2015." *Earth's Future* 10 (5). <https://doi.org/10.1029/2021ef002566>.
- Wu, G., Z. Liu, L. Zhang, J. Chen, and T. Hu. 2010. "Long-term Fencing Improved Soil Properties and Soil Organic Carbon Storage in an Alpine Swamp Meadow of Western China." *Plant and Soil* 332 (1-2): 331–337. <https://doi.org/10.1007/s11104-010-0299-0>.
- Xia, J., S. Niu, P. Ciais, I. A. Janssens, J. Chen, C. Ammann, A. Arain, et al. 2015. "Joint Control of Terrestrial Gross Primary Productivity by Plant Phenology and Physiology." *Proceedings of the National Academy of Sciences of the United States of America* 112 (9): 2788–2793. <https://doi.org/10.1073/pnas.1413090112>.
- Xiao, C., Y. Wang, M. Yan, and J. Chiwiikem Chiaka. 2024. "Impact of Cross-Border Transportation Corridors on Changes of Land use and Landscape Pattern: A Case Study of the China-Laos Railway." *Landscape and Urban Planning* 241:104924. <https://doi.org/10.1016/j.landurbplan.2023.104924>.
- Xie, J., H. Gu, and G. Yin. 2024. "Drought Decreased Annual Cumulative Carbon Uptake in Southwest China Mainly through Its Influence on Phenology Rather than Physiology." *Ecological Indicators* 158:111359. <https://doi.org/10.1016/j.ecolind.2023.111359>.
- Yang, S., L. Zhang, and G. Zhu. 2023. "Effects of Transport Infrastructures and Climate Change on Ecosystem Services in the Integrated Transport Corridor Region of the Qinghai-Tibet Plateau." *Science of the Total Environment* 885:163961. <https://doi.org/10.1016/j.scitotenv.2023.163961>.
- Yang, W., H. Kobayashi, C. Wang, M. Shen, J. Chen, B. Matsushita, Y. Tang, et al. 2019. "A Semi-analytical Snow-Free Vegetation Index for Improving Estimation of Plant Phenology in Tundra and Grassland Ecosystems." *Remote Sensing of Environment* 228:31–44. <https://doi.org/10.1016/j.rse.2019.03.028>.
- Yao, T. 2019. "Tackling on Environmental Changes in Tibetan Plateau with Focus on Water, Ecosystem and Adaptation." *Science Bulletin* 64 (7): 417–417. <https://doi.org/10.1016/j.scib.2019.03.033>.

- Yin, G., X. Yan, D. Ma, J. Xie, R. Chen, H. Pan, W. Zhao, et al. 2023. "Polar-facing Slopes Showed Stronger Greening Trend than Equatorial-facing Slopes in Tibetan Plateau Grasslands." *Agricultural and Forest Meteorology* 341:109698. <https://doi.org/10.1016/j.agrformet.2023.109698>.
- Yu, X., R. Orth, M. Reichstein, M. Bahn, A. Klosterhalfen, A. Knohl, F. Koebisch, et al. 2022. "Contrasting Drought Legacy Effects on Gross Primary Productivity in a Mixed versus Pure Beech Forest." *Biogeosciences* 19 (17): 4315–4329. <https://doi.org/10.5194/bg-19-4315-2022>.
- Zeng, Z., W. Wu, Q. Ge, Z. Li, X. Wang, Y. Zhou, Z. Zhang, et al. 2021. "Legacy Effects of Spring Phenology on Vegetation Growth under Preseason Meteorological Drought in the Northern Hemisphere." *Agricultural and Forest Meteorology* 310:108630. <https://doi.org/10.1016/j.agrformet.2021.108630>.
- Zhang, W., G. Yu, Z. Chen, X. Zhu, L. Han, Z. Liu, Y. Lin, et al. 2022. "Photosynthetic Capacity Dominates the Interannual Variation of Annual Gross Primary Productivity in the Northern Hemisphere." *Science of the Total Environment* 849:157856. <https://doi.org/10.1016/j.scitotenv.2022.157856>.
- Zhang, Y. 2022. "Naqu Flux Observation Data (2018)" (dataset). National Tibetan Plateau / Third Pole Environment Data Center. <https://doi.org/10.11888/TERRE.tpdc.272862>.
- Zhou, D., L. Zhang, L. Huang, J. Fan, Y. Li, and H. Zhang. 2023. "Satellite Evidence for Small Biophysical Effects of Transport Infrastructure in the Qinghai-Tibet Plateau." *Journal of Cleaner Production* 416:138002. <https://doi.org/10.1016/j.jclepro.2023.138002>.
- Zhou, H., X. Yang, C. Zhou, X. Shao, Z. Shi, H. Li, H. Su, et al. 2023. "Alpine Grassland Degradation and Its Restoration in the Qinghai – Tibet Plateau." *Grasses* 2 (1): 31–46. <https://doi.org/10.3390/grasses2010004>.
- Zhou, S., Y. Zhang, K. K. Caylor, Y. Luo, X. Xiao, P. Ciais, Y. Huang, and G. Wang. 2016. "Explaining Inter-annual Variability of Gross Primary Productivity from Plant Phenology and Physiology." *Agricultural and Forest Meteorology* 226–227:246–256. <https://doi.org/10.1016/j.agrformet.2016.06.010>.